Available online at www.sciencedirect.com
SCIENCE DIRECT®
Journal of Power Sources 142 (2005) 211–222
JOURNAL OF POWER SOURCES
www.elsevier.com/locate/jpowsour

Dynamic modeling of single tubular SOFC combining heat/mass transfer and electrochemical reaction effects

X. Xue[a], J. Tang[a,*], N. Sammes[a], Y. Du[b]

[a] *Department of Mechanical Engineering, University of Connecticut, 191 Auditorium Road, Unit 3139, Storrs, CT 06269, USA*
[b] *Connecticut Global Fuel Cell Center, University of Connecticut, 44 Weaver Road, Unit 5233, Storrs, CT 06269, USA*

Received 22 September 2004; accepted 16 November 2004
Available online 5 January 2005

Abstract

In this paper, a dynamic model of a single tubular solid oxide fuel cell (SOFC) unit is developed using the control volume (CV) approach. The heat transfer, species transportation, and electrochemical reaction effects are taken into account in a collective manner. Using this model, we study the spatial distributions of a series of state variables under both steady-state and transient operations and evaluate the system dynamic behavior. The analysis shows that there exists non-uniform current contribution and Nernst potential distribution along the longitudinal direction, caused by the non-uniform fuel/gas partial pressures along the flow direction and the temperature distribution in the anode/cathode channel and cell body, for example. The classical Nernst potential relation is revised to capture the characteristics of the fuel cell under time varying external load voltage. Comprehensive numerical simulations are carried out to explore the underlying dynamic properties in typical SOFC operations. The numerical study is also correlated to experimental results such as the polarization curve and power density, which shows good agreement.

Keywords: SOFC; Dynamic modeling; Tubular; Heat transfer; Mass transfer

1. Introduction

Solid oxide fuel cells (SOFCs) are very promising types of high temperature fuel cells currently being considered for commercial power source applications. Since the electrolyte is a layer of ceramic material with high temperature-endurable porous media electrodes, the SOFC can generally operate at high temperature range (800–1000 °C). High operating temperature can lead to some advantages, such as high oxide-ion conductivity of the solid oxide electrolyte, high rate of reaction kinetics and hence high-energy conversion efficiency, flexibility of fuel type due to reforming capability of hydrocarbons, and the high temperature of the exiting gas which could be recycled for other applications. On the other hand, the high temperature operating condition also imposes some challenges which include potential thermal fatigue failure of the cell material, sealing under high temperature, and the associated control mechanism/power required to maintain the operation.

Planar and tubular geometries are the two most popular forms of SOFC. The tubular type SOFC is relatively mature in terms of design and sealing, while the planar type shows better manufacturability. The core of a SOFC consists of a porous cathode electrode, electrolyte, and porous anode electrode assembly (PEN), where the electrochemical reaction takes place and electrical energy and heat are generated directly from the species chemical energy [1,2]. The environmental condition of the electrochemical reaction has direct effects on the efficiency of the fuel cell. Besides the physical properties of the PEN, the cell temperature, partial pressures of hydrogen, oxygen and vapor, etc. all play important roles in the electrochemical reaction. In order to analyze the complicated interactions between the various factors and

* Corresponding author. Tel.: +1 860 486 5911; fax: +1 860 486 5088.
E-mail address: jtang@engr.uconn.edu (J. Tang).

0378-7753/$ – see front matter © 2004 Elsevier B.V. All rights reserved.
doi:10.1016/j.jpowsour.2004.11.023

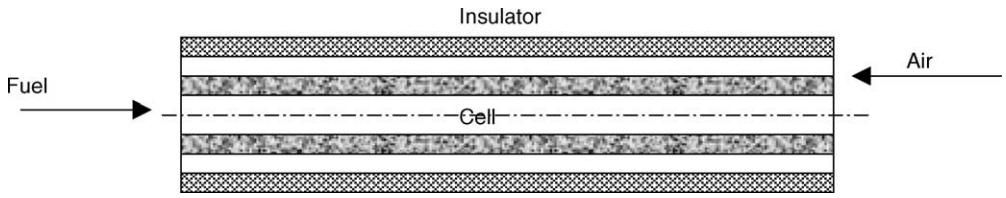

Fig. 1. Tubular cell configuration.

to optimize the system performance, there has been significant interest in developing mathematical models for SOFC [3–9]. Li and Chyu [3] proposed a 2D steady-state model for a tubular SOFC in a stack by assuming that heat and species are not exchanged between a cell and its neighbors. The model did not consider the radiation effect among cells. Similarly, Nagata et al. [4] investigated output characteristics of a 1D steady-state tubular type SOFC whereas the radiation effect is included. Haynes [5] developed a transient model to capture the heat transfer effects. However, some conditions assumed in that research were not consistent with the essential characteristics of the transient behavior. For example, the inlet gas/fuel mole fraction was assumed constant. Ota et al. [6] explored the dynamic behavior of a micro-tube SOFC. In that model, they imposed the incompressible assumption of gases and the viscous effect was not considered. Such effect, nevertheless, could have significant impact on species partial pressure distribution along the flow direction especially for the micro-tube, and in turn influence the voltage and current distributions along the cell. In addition, the heat conduction between the defined slices was also neglected in that model. Cooper et al. [7] proposed a steady-state model for the reaction and species transport process of a tubular type SOFC. Since only steady-state operation is considered, the energy equation is not involved in the modeling and analytical solution with asymptotic expansion can be obtained. It is worth noting that the electrochemical characteristics of the cell are generally treated as an equivalent circuit model, and the Nernst potential is usually regarded as a potential source [3,4,6].

It is the goal of this study to develop a dynamic model of the SOFC that is capable of characterizing the transient/time- and spatial-dependent properties of critical state variables. Although a lot of work has been dedicated to the steady-state performance evaluation [3,4,7–9], the inclusion of transient dynamics significantly complicates the model development. It appears that the direct integration of time dependency into the high precision steady-state model (such as the one given in [3]) could lead to insurmountable computational cost. This is especially true for single tubular SOFCs packed in a stack. Clearly, the real challenge is to develop a model that can be sufficiently utilized in system optimization and dynamic control while being computationally tractable. In this research, building upon the previous studies on dynamic modeling of SOFC and using the control volume (CV) approach, we develop a discrete SOFC model which incorporates thoroughly the effects of conduction, convection, radiation, species transportation, and electrochemical reaction. In modeling the electrochemical reaction, we use a revised Nernst potential relation to characterize the unique flip-flop behavior in a SOFC under time varying operating conditions. This model will allow us to carry out detailed analysis on current/voltage distributions and temperature and, for example, fuel/gas partial pressure distributions.

2. Modeling of SOFC

2.1. Single tubular SOFC configuration

We consider an anode-supported single tubular fuel cell illustrated in Fig. 1 [1]. The internal cylinder is the cell body, covered by a layer of thermal insulator. The fuel and oxygen flow in opposite directions, which could make the heat/temperature distribution along the cell more uniform. Three basic SOFC designs have been explored in the open literature, the electrolyte-supported, the cathode- and anode-supported designs. Since the electrolyte-supported SOFC exhibits very high electrolyte resistance under moderate temperature, the operation must be at very high temperature ($\sim$1000 °C). Electrode-supported designs are better suited for lower temperature operation. It has been argued that an anode-supported SOFC could have better cell output power [1,2]. Without loss of generality, in this paper we focus our attention on the anode-supported SOFC. This modeling strategy can be easily extended to other SOFC designs.

2.2. Modeling of heat transfer effects

A SOFC involves complicated heat transfer, species transportation, and electrochemical effects which are highly interactive. In order to make the model tractable while capturing the fundamental dynamic behavior, we reduce the problem to a quasi-2D analysis based on the changes along the gas flow direction using the control volume (CV) approach [4–6,8]. In other words, while the flow field within each channel is considered as 1D respectively, the cross-sectional effects (e.g., heat transfer, species transportation, etc.) between the two concentric channels are fully taken into account. As shown in Fig. 2, the cell is divided into serial segments by the planes perpendicular to fuel flow direction. Each segment includes four CVs, i.e., anode CV, cell CV, cathode CV, and thermal insulator CV. Within the control volume, we assume uniform physical properties. It should be noted that the physical

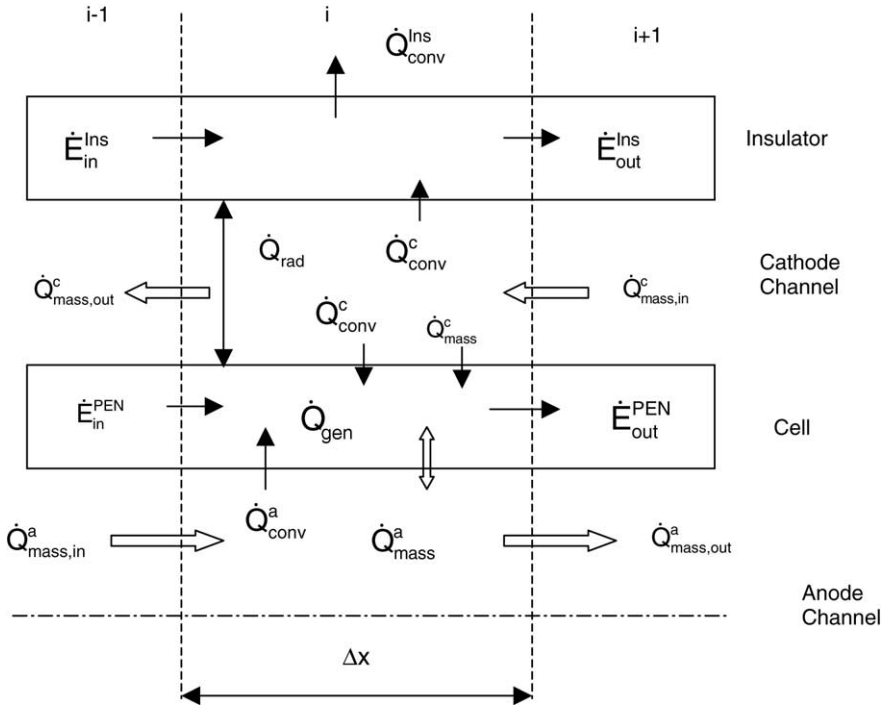

Fig. 2. Mass and energy balance CV illustration.

properties in different CVs are not necessarily the same. The electrochemical reactions take place in the cell (PEN). Due to the high operating temperature, all the water produced by the electrochemical reactions is assumed to be in the vapor state. Here we assume an ideal gas mixture within the cell, which means that each mixture component behaves as an ideal gas as if it were alone [10]. For the control volumes of the PEN and insulator, only the energy balance equations are needed because these two control volumes are made of solid materials, while the control volumes of gas/fuel must satisfy the balance equations of mass/species, momentum and energy.

2.2.1. Mass/species conservation equation

First we consider the fuel/gas CV. The mass/species balance equation for this CV satisfies [11]:

$$V_i \frac{\partial \rho_i}{\partial t} + (Y\rho u A)_{i-1} - (Y\rho u A)_{i+1} = \dot{m}_{\text{surf}} \tag{1}$$

where V is the control volume, ρ the species density within the CV, Y the species mass fraction, A the cross-section area, u the bulk gas flow speed, $\dot{m}_{\text{surf}}$ the net species mass flux through the connecting surface between neighboring CVs, and the subscript i designates the ith CV.

For the ith anode channel CV, the entering species from the $(i-1)$th CV and the leaving species to the $(i+1)$th CV are hydrogen and vapor. The diffusion species include the hydrogen for the electrochemical reaction (diffusing into the anode electrode) and vapor (generated by the electrochemical reaction and diffusing out from anode electrode). For the cathode channel CV, the flow stream species include oxygen and nitrogen from air or pure oxygen. The oxygen is the only involved species diffusing into the cathode electrode under electrochemical reaction. These can be characterized by plugging relevant species parameters into Eq. (1), which will yield a set of equations that describes the mass/species conservation within each CV.

2.2.2. Momentum equation

Generally, the flow field also satisfies the momentum equation [11]:

$$V_i \frac{\partial \left(\sum u\rho_k Y_k\right)}{\partial t} + \left(\sum u\rho_k Y_k u A\right)_{i-1} - \left(\sum u\rho_k Y_k u A\right)_i = \sum F_{\text{longitudinal}} \tag{2}$$

For the anode channel CV, the entering/leaving momentum is caused by main flow stream hydrogen and water vapor. As compared to the total mass of main flow stream, the mass directly involved in the electrochemical reaction is small, and thus the momentum effect on the main flow stream caused by such electrochemical reaction is negligible. The cathode channel that involves the oxygen and nitrogen flows is modeled using a similar assumption. Again, when plugging the respective species parameters into Eq. (2), we can get a set of equations that characterize the momentum balance within the CV.

2.2.3. Energy balance equation

Consider Fig. 2. The energy balance equation for the fuel/gas CV (corresponding to the anode channel) can be

expressed as follows [10,11]:

$$V_i \frac{\partial\left(\sum_k e_k \rho_k\right)_i}{\partial t} = (\dot{Q}^{\mathrm{a}}_{\mathrm{mass,in}})_{i-1} - (\dot{Q}^{\mathrm{a}}_{\mathrm{mass,out}})_{i+1} - (\dot{Q}^{\mathrm{a}}_{\mathrm{conv}})_i - (\dot{Q}^{\mathrm{a}}_{\mathrm{mass,diff}})_i \quad (3a)$$

where e is the specific internal energy within the CV, $\dot{Q}^{\mathrm{a}}_{\mathrm{mass,in}}$ and $\dot{Q}^{\mathrm{a}}_{\mathrm{mass,out}}$ the energy transfer rates along the flow stream, $\dot{Q}^{\mathrm{a}}_{\mathrm{conv}}$ the convective heat transfer rate between the gas CV and the PEN/thermal insulator CV, and $\dot{Q}^{\mathrm{a}}_{\mathrm{mass,diff}}$ is the heat convection rate between the gas CV and the PEN/insulator CV due to mass diffusion. The radiation heat transfer between the gas CV and the solid CV is not considered.

For the anode channel, the flow stream energy transfer rates between the neighboring CVs can be represented as, respectively:

$$(\dot{Q}^{\mathrm{a}}_{\mathrm{mass,in}})_{i-1} = \left(\sum_k Y_k e_k \rho_k u A\right)_{i-1} \quad (3b)$$

$$(\dot{Q}^{\mathrm{a}}_{\mathrm{mass,out}})_{i+1} = \left(\sum_k Y_k e_k \rho_k u A\right)_{i} \quad (3c)$$

The convection heat transfer rate between the gas CV and solid CV is given as [12]:

$$(\dot{Q}^{\mathrm{a}}_{\mathrm{conv}})_i = h_i A^{\mathrm{c}}_i [(T_{\mathrm{g}})_i - (T_{\mathrm{s}})_i] \quad (3d)$$

where h is the convective heat transfer coefficient, A^{c} the circumferential area of the CV, T_{g} the gas temperature within the CV, and T_{s} is the temperature of the solid CV adjacent to the gas CV.

The heat transfer due to the mass diffusion effect includes the gas diffusion entering and leaving the PEN [12]:

$$(\dot{Q}^{\mathrm{a}}_{\mathrm{mass,diff}})_i = \sum_k M_k \frac{I_i}{n_k F} (c_p)_k (T_{\mathrm{g}} - T_{\mathrm{s}})_i \quad (3e)$$

where M is the species molecular mass, n the number of electrons per mole of the kth reactant species, I the current contribution of the corresponding CV segment, F the Faraday's constant, and c_p is the specific heat of species. For the anode channel CV, hydrogen and vapor are involved in Eq. (3e), while only oxygen is involved in the cathode electrode diffusion and electrochemical reaction.

The energy balance in the CVs of PEN and insulator is given as

$$(\rho V c_p)_i \frac{\mathrm{d}T_i}{\mathrm{d}t} = (\dot{E}_{\mathrm{in}})_{i-1} + \sum (\dot{Q}_{\mathrm{conv}})_i + \sum (\dot{Q}_{\mathrm{mass}})_i + (\dot{Q}_{\mathrm{rad}})_i - (\dot{E}_{\mathrm{out}})_{i+1} + (\dot{Q}_{\mathrm{gen}})_i \quad (4a)$$

where $\dot{E}_{\mathrm{in}}$ and $\dot{E}_{\mathrm{out}}$ are the heat conduction effects due to the adjacent solid CVs, $\dot{Q}_{\mathrm{conv}}$ and $\dot{Q}_{\mathrm{mass}}$ are given in Eqs. (3d) and (3e), $\dot{Q}_{\mathrm{rad}}$ the radiation heat transfer rate between the cell and the thermal insulator, and $\dot{Q}_{\mathrm{gen}}$ is the heat generation rate within the CV due to electrochemical reaction and current flow. It should be noted that since the PEN and insulator CVs are composed of solid materials, only the energy balance equation is needed. The heat conduction effects can be quantified as follows [11]:

$$(\dot{E}_{\mathrm{in}})_{i-1} = kA \frac{T_{i-1} - T_i}{\Delta x} \quad (4b)$$

$$(\dot{E}_{\mathrm{out}})_{i+1} = kA \frac{T_i - T_{i+1}}{\Delta x} \quad (4c)$$

where k is the material conductivity, and Δx is the segment length.

In this study, we take into account the radiation effect between the cell CV and its adjacent thermal insulator CV. Such radiation heat transfer can be approximated by using the infinite length concentric cylinder theory [12]:

$$(\dot{Q}_{\mathrm{rad}})_i = \frac{\sigma A^{\mathrm{c}}_i (T^4_{\mathrm{Ins}} - T^4_{\mathrm{PEN}})_i}{1/\varepsilon_{\mathrm{PEN}} + (r_{\mathrm{PEN}}/r_{\mathrm{Ins}})((1/\varepsilon_{\mathrm{Ins}}) - 1)} \quad (4d)$$

where σ is the Stefan–Boltzmann constant, r_{PEN} and r_{Ins} are the outside and inside diameters of the PEN and insulator, respectively, and ε is the surface emissivity.

The electrochemical reaction heat only occurs in the PEN layers [4,14]:

$$(\dot{Q}_{\mathrm{gen}})_i = M_{\mathrm{H_2}} \frac{I_i}{2F} \Delta H_{\mathrm{H_2}} + I_i^2 (R_{\mathrm{A}} + R_{\Omega} + R_{\mathrm{C}})_i \quad (4e)$$

where $\Delta H_{\mathrm{H_2}}$ is the low heating value of hydrogen, R_{A} is the anode overpotential resistance, R_{C} is the cathode overpotential resistance, and R_{Ω} is the ohmic resistance.

The above derivation completes the energy balance characterization of the anode channel, the cell body, and the thermal insulator. For the cathode channel, the general description is very similar to that of the anode channel. In addition to the species difference, however, it should be noted that for the cathode channel, due to the reverse in flow direction, the order of CVs in Eqs. (1)–(3) should also be reversed, i.e., $i+1$ is the upstream and $i-1$ is the down stream. Also, for the cathode channel CV, the convection involves that between the PEN and the cathode channel and that between the insulator and the cathode channel, while the convection for the anode channel only involves that between the PEN and the anode channel.

2.3. Modeling of electrochemical reaction

A SOFC is an electrochemical device that converts the chemical energy into electrical energy directly. At the cathode side, the oxygen diffuses through the electrode and reaches the electrode/electrolyte interface, where the oxygen is electrochemically reduced into oxygen ions by consuming the electrons transported through the external circuit. The oxygen ion is transported through the electrolyte to the anode side. The hydrogen in the anode channel diffuses through

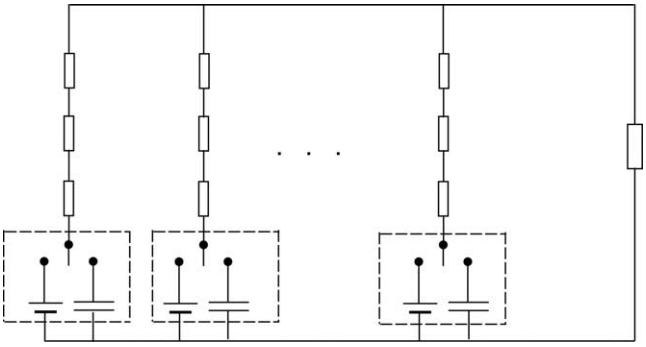

Fig. 3. Equivalent circuit of SOFC.

the electrode and reaches the electrode/electrolyte interface, where the oxygen ions react with hydrogen to form water and electrons. Electricity is generated by the formed electrons at the anode side. The oxidation of the hydrogen yields the Nernst potential equation [2,12,13]:

$$E = \frac{-\Delta G^\circ}{2F} + \frac{RT}{2F}\ln\left(\frac{P_{H_2} P_{O_2}^{1/2}}{P_{H_2O}}\right) \tag{5}$$

where ΔG° is the variation of standard state Gibbs' free energy of oxidation reaction of the hydrogen, R the universal gas constant, T the temperature at the reaction site, P_{H_2} and P_{H_2O} are the ratios of the hydrogen and water vapor partial pressures at the anode electrode/electrolyte interface over the standard atmosphere pressure respectively, and P_{O_2} is the oxygen counterpart at the cathode electrode/electrolyte interface.

The operating cell potential is generally lower than the Nernst potential, which is typically caused by the ohmic, concentration and activation polarizations. Based upon experimental characterizations, the anode and cathode equivalent resistances are quantified as [13,14]:

$$R_A = \left[\frac{4F}{RT} k_A \left(\frac{P_{H_2}}{P}\right)^{0.25} \exp\left(-\frac{U_A}{RT}\right)\right]^{-1} \tag{6}$$

$$R_C = \left[\frac{4F}{RT} k_C \left(\frac{P_{O_2}}{P}\right)^{0.25} \exp\left(-\frac{U_C}{RT}\right)\right]^{-1} \tag{7}$$

where U_A and U_C are the activation energy of the anode and cathode, respectively, and k_A and k_C are the pre-exponential factors that are obtained experimentally.

With the CV approach as a basis, the equivalent fuel cell circuit [3,4,6,14] can be formed as shown in Fig. 3. Each segment of the fuel cell constitutes a sub-fuel cell. It is assumed that the neighboring sub-fuel cells have no direct current flow between each other through either the electrolyte or the anode/cathode electrodes, since the internal resistance between them is much larger.

Traditionally, the Nernst potential of a sub-fuel cell is simply treated as a potential/voltage source [3,4,6,14], and the current and voltage in the circuit is thus calculated through

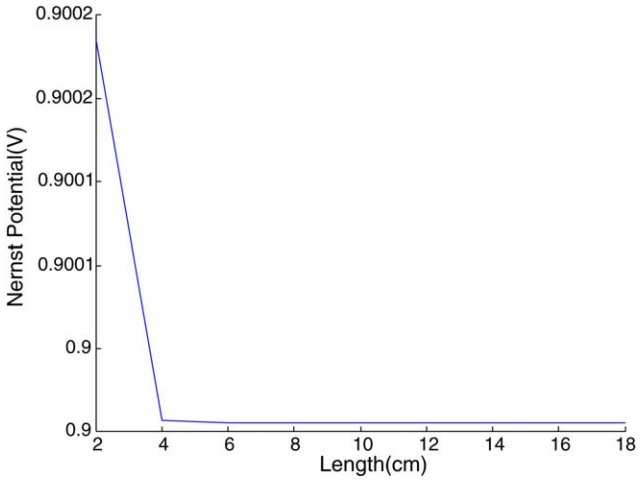

Fig. 4. Illustration of modified fuel cell Nernst potential.

Kirchhoff's law. It is worth noting that a fuel cell can be treated as a voltage source only if the Nernst potential is accumulated high enough so that it can deliver the external load potential requested. If the external load potential is higher than the fuel cell Nernst potential, the fuel cell will have to switch the role from potential source to an energy storage element [15]. This can be illustrated by the simulation result of a single tubular SOFC as given in Fig. 4 (detailed discussions will be given in Section 3). As will be explained later, the Nernst potential distribution of a SOFC decays along the longitudinal direction. Suppose the output voltage stays at a constant value, for example, 0.9 V, as shown in Fig. 4. The Nernst potentials at some segments are lower than the external load voltage. In this case, instead of the Nernst potential providing the electrical energy, the external voltage or the Nernst potentials at other segments of the SOFC will provide charge to the sub-cells until the relevant potentials are high enough to satisfy the external voltage requirement. In the current case, the downstream Nernst potentials will finally reach the level of the external load voltage as shown in Fig. 4. Depending on the levels of sub-cell Nernst potentials and the external load voltage, the role of sub-cells could flip back and forth. Under these considerations, in this research we consider the sub-fuel cell as a combined effect of the Nernst potential and capacitor:

$$E_{\text{Nernst}} = \begin{cases} E | E = -\dfrac{\Delta G^\circ}{2F} + \dfrac{RT}{2F}\ln\left(\dfrac{P_{H_2} P_{O_2}^{1/2}}{P_{H_2O}}\right), & E \geq V_{\text{out}} \\ V | \dfrac{dV}{dt} = \dfrac{1}{RC}(V_{\text{out}} - V), & E < V_{\text{out}} \end{cases} \tag{8}$$

where V_{out} is the terminal output voltage, E the original Nernst potential produced by the electrochemical reaction, R the total resistance consisting of concentration, activation and ohmic resistances, C the capacitance formed by sand-

wiched electrode and electrolyte of sub-fuel cell, and V the sub-fuel cell potential if the original Nernst potential is less than the output voltage.

The Kirchhoff's voltage and current laws are then employed to calculate the current and other related variables, i.e.,

$$E_{\text{out}} = (E_{\text{Nernst}})_i - (R_{\text{A}} + R_{\Omega} + R_{\text{C}})_i I_i \tag{9a}$$

$$I_{\text{out}} = \sum_i I_i \tag{9b}$$

where E_{out} and I_{out} are the load voltage and the load current, respectively, $(E_{\text{Nernst}})_i$ and I_i are the sub-fuel cell Nernst potential and the associated current. The three polarization resistances are calculated based on the instant conditions of the corresponding sub-cell.

Table 1
Parameters used in simulation

Symbol	Meaning	Value	Reference
L	Fuel cell length	200 mm	
n	Segment number	10	
Δx	Segment length	20 mm	
r_{a}	Inside radius of the cell	3.1 mm	
r_{b}	Outside radius of the cell	3.9 mm	
r_{c}	Inside radius of the insulator	7.0 mm	
r_{d}	Outside radius of the insulator	9.0 mm	
M_{H_2}	Molecule weight of hydrogen	$2.016\,\text{g mol}^{-1}$	[13]
$c_{p\text{H}_2}$	Specific heat of hydrogen (constant pressure)	$14821\,\text{J kg}^{-1}\,\text{K}^{-1}$	[10]
R_{H_2}	Hydrogen gas constant	$4124.3\,\text{J kg}^{-1}\,\text{K}^{-1}$	[13]
c_{vH_2}	Specific heat of hydrogen (constant volume)	$10697\,\text{J kg}^{-1}\,\text{K}^{-1}$	[10]
ρ_{H_2}	Hydrogen density at 900 K	$0.02723\,\text{kg m}^{-3}$	[10]
μ_{H_2}	Dynamic viscosity of hydrogen	$18.78 \times 10^{-6}\,\text{kg m}^{-1}\,\text{s}^{-1}$	[10]
ΔH	Low heating value of hydrogen	$1.196 \times 10^{8}\,\text{J}$	Well known
$M_{\text{H}_2\text{O}}$	Molecule weight of water vapor	$18.02\,\text{g mol}^{-1}$	[13]
$c_{p\text{H}_2\text{O}}$	Specific heat of water vapor (constant pressure)	$2186\,\text{J kg}^{-1}\,\text{K}^{-1}$	[10]
$R_{\text{H}_2\text{O}}$	Water vapor gas constant	$188.5\,\text{J kg}^{-1}\,\text{K}^{-1}$	[13]
$c_{v\text{H}_2\text{O}}$	Specific heat of water vapor (constant volume)	$1997.5\,\text{J kg}^{-1}\,\text{K}^{-1}$	[10]
$\rho_{\text{H}_2\text{O}}$	Water vapor density at 850 K	$0.2579\,\text{kg m}^{-3}$	[10]
$\mu_{\text{H}_2\text{O}}$	Dynamic viscosity of water vapor	$29.69 \times 10^{-6}\,\text{kg m}^{-1}\,\text{s}^{-1}$	[10]
M_{O_2}	Molecule weight of oxygen	$32\,\text{g mol}^{-1}$	[13]
$c_{p\text{O}_2}$	Specific heat of oxygen (constant pressure)	$988.1\,\text{J kg}^{-1}\,\text{K}^{-1}$	[10]
R_{O_2}	Oxygen gas constant	$259.8\,\text{J kg}^{-1}\,\text{K}^{-1}$	[13]
$c_{v\text{O}_2}$	Specific heat of oxygen (constant volume)	$728.3\,\text{J kg}^{-1}\,\text{K}^{-1}$	[10]
ρ_{O_2}	Oxygen density at 550 K	$0.7096\,\text{kg m}^{-3}$	[10]
μ_{O_2}	Dynamic viscosity of oxygen	$31.97 \times 10^{-6}\,\text{kg m}^{-1}\,\text{s}^{-1}$	[10]
h_{a}	Convective coefficient in anode channel	$2987\,\text{W m}^{-2}\,\text{K}^{-1}$	[a]
h_{c}	Convective coefficient in cathode channel	$1322.8\,\text{W m}^{-2}\,\text{K}^{-1}$	[a]
h_{∞}	Convective coefficient insulator/surrounding	$10\,\text{W m}^{-2}\,\text{K}^{-1}$	[10]
ρ_{PEN}	Average density of PEN	$6337.3\,\text{kg m}^{-3}$	[12]
$c_{p\text{PEN}}$	Average specific heat of PEN	$594.3\,\text{J kg}^{-1}\,\text{K}^{-1}$	[12]
k_{PEN}	Average thermal conductivity of PEN	$2.53\,\text{W m}^{-1}\,\text{K}^{-1}$	[12]
ε_{PEN}	Average emissivity of PEN	0.33	[10]
ρ_{Ins}	Density of insulator	$480\,\text{kg m}^{-3}$	[10]
$c_{p\text{Ins}}$	Specific heat of insulator	$1047\,\text{J kg}^{-1}\,\text{K}^{-1}$	[10]
k_{Ins}	Thermal conductivity of insulator	$0.059\,\text{W m}^{-1}\,\text{K}^{-1}$	[10]
ε_{Ins}	Thermal emissivity of insulator	0.09	[10]
σ	Stefen–Boltzmann constant	$5.669 \times 10^{-8}\,\text{W m}^{-2}\,\text{K}^{-4}$	[10]
P_{s}	Fuel/gas source pressure	$3.0 \times 10^{5}\,\text{Pa}$	[b]
T_{s}	Fuel/gas source temperature	1073 K	[b]
T_{∞}	Surrounding temperature	303 K	[b]
$K_{\text{a\_in}}$	Inlet flow coefficient of anode channel	$8.7641 \times 10^{-10}\,\text{kg Pa}^{-1}\,\text{s}^{-1}$	[c]
$K_{\text{a\_out}}$	Outlet flow coefficient of anode channel	$4.3821 \times 10^{-7}\,\text{kg Pa}^{-1}\,\text{s}^{-1}$	[c]
$K_{\text{c\_in}}$	Inlet flow coefficient of cathode channel	$3.1626 \times 10^{-8}\,\text{kg Pa}^{-1}\,\text{s}^{-1}$	[c]
$K_{\text{c\_out}}$	Outlet flow coefficient of cathode channel	$1.5813 \times 10^{-5}\,\text{kg Pa}^{-1}\,\text{s}^{-1}$	[c]
R_{Ω}	Fuel cell ohmic resistance	$0.0257\,\Omega$	[10]
E_{A}	Anode activation energy	$110\,\text{kJ mol}^{-1}$	[10]
E_{C}	Cathode activation energy	$160\,\text{kJ mol}^{-1}$	[10]
k_{A}	Anode pre-exponential factor	$2.13 \times 10^{8}\,\text{A m}^{-2}$	[10]
k_{C}	Cathode pre-exponential factor	$1.49 \times 10^{10}\,\text{A m}^{-2}$	[10]

[a] The coefficients are calculated by assuming a fully developed laminar flow at constant wall temperature [6].
[b] Parameters are assumed.
[c] Parameters are assumed and adjustable.

3. Results and discussion

The above section presents a complete set of mathematical relations governing the transient dynamic behavior of SOFC. Using these equations, we develop a Matlab code to simulate the single tubular fuel cell operation. All physical and geometrical parameters used in the simulation are given in Table 1. The cell is divided into ten segments, where the two end segments do not involve the fuel/gas diffusion and electrochemical reaction. The mass flow rate is estimated using the nozzle equation [16]. The model is highly nonlinear with distributed parameters. We first evaluate the steady-state solution using an iterative procedure and the dynamic response is then calculated using stiff solver ode15s with calculated initial conditions.

3.1. Correlation with steady-state experimental results

We start by verifying the dynamic model using a correlation of the available experimental data. A single tubular SOFC tested is a nickel and yttria-stabilized zirconia (Ni–YSZ) cermet anode-supported tube with a thin YSZ electrolyte coat and a thin lanthanum strontium magnate (LSM) cathode [1]. The dimensions and the relevant physical properties of the cell are given in Table 1. In the experiment, the fuel cell temperature is kept at 850 °C by using an electrical furnace coupled with a temperature control unit. The fuel flowing through the anode channel is pure hydrogen, whereas the oxygen is obtained directly from the air to facilitate the electrochemical reaction. In this simplified experiment, the cell does not have the thermal insulator layer. We specify the load current and correspondingly measure the output voltage. This process is repeated for current density from 0 to 0.36 A cm^{-2} and the experimental polarization curve and power density curve are obtained. In order to carry out the correlation between the experiment and the simulation, we insert the experimental parameters and conditions into the dynamic model. The insulator in the model is removed to fit the experimental condition, and the cathode channel now is treated as ambient. As the temperature of the cell is maintained as constant, the energy balance equation of the cell body is not involved in the simulation. Under these assumptions, we perform steady-state numerical simulation, and the polarization curve and the power density curve comparisons are given in Figs. 5 and 6. It can be clearly observed that the simulation results have a consistent trend when compared to experimental data and the model can predict the steady-state behavior under the specific experimental conditions reasonably well.

3.2. Steady-state performance analysis

A more detailed analysis is carried out to explore the underlying dynamic properties under typical SOFC operations. The following analysis is performed on a complete cell unit where the geometric and material properties are listed in Table 1. It should be noted that the key parameters are those

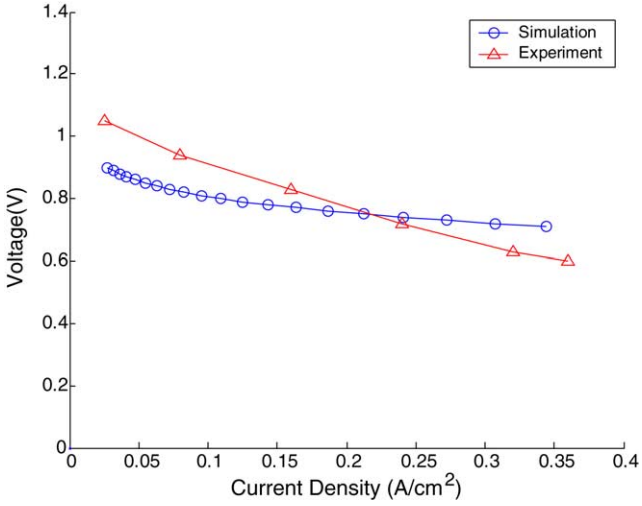

Fig. 5. Experiment and simulation comparison of polarization curve.

used in the experimental study mentioned above, whereas the cell now has an insulating layer and operates under standard conditions (without a temperature control unit). The species parameters are selected based on previous studies [10,12].

To evaluate the external load voltage effect on the performance of the tubular fuel cell, a series of step load voltages (four levels, 0.5, 0.7, 0.9, and 1.1 V) are employed as the input to the system, and the corresponding steady-state results are illustrated in Figs. 7–14. Fig. 7 shows the Nernst potential distribution along the longitudinal direction of the fuel cell. When the external load voltage is 0.5 V, the Nernst potentials of all sub-fuel cells are higher than the external load voltage, and thus the entire tubular fuel cell contributes current to the external circuit based on the Kirchhoff's voltage law. In other words, under such a scenario the Nernst potentials of all sub-cells obey the first equation shown in Eq. (8). This result can be validated by the current distribution given in Fig. 8, where it can be seen that all sub-cells contribute (positive) current. When the load voltage increases to 0.7 V, the Nernst

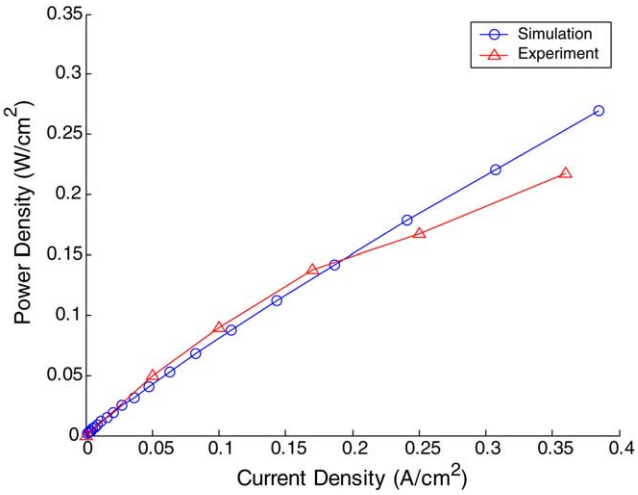

Fig. 6. Experiment and simulation comparison of output power.

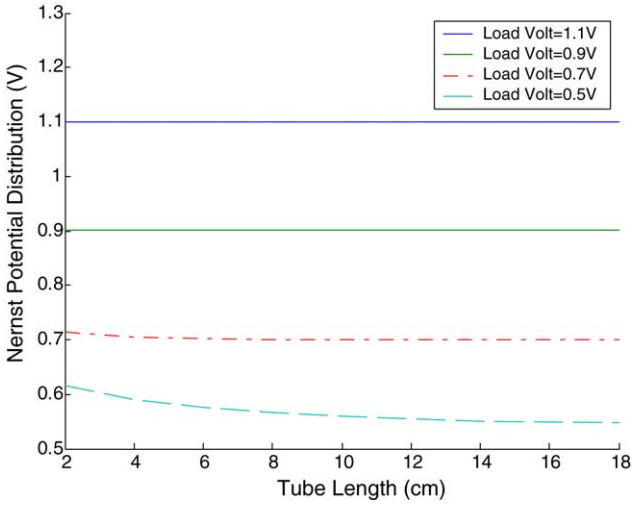

Fig. 7. Fuel cell Nernst potential distribution along the longitudinal direction.

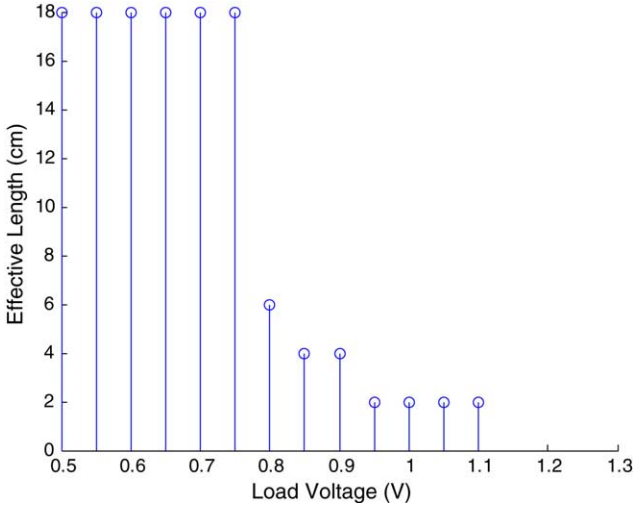

Fig. 9. Effective length of fuel cell for different load voltages.

potentials at the downstream (in the direction of fuel flow) segments of the tubular fuel cell become very close to the load voltage. Consequently, while the upstream segments of the fuel cell still contributes current, the current contributions from the down stream segments are close to zero, as shown in Fig. 8. This becomes more obvious as the load voltage further increases to 0.9 and 1.1 V. In these cases, while the Nernst potentials of several upstream segments are greater than the load voltage, the Nernst potentials of the majority of segments (at downstream direction) are not large enough as compared to the load voltage. Correspondingly, the current contributions from almost the entire tubular fuel cell are zero. If the external load voltage increases further, the fuel cell will not be able to generate current but instead behave like an energy storage element, i.e., a capacitor. This can be demonstrated by plotting the effective length of the tubular fuel cell (the length of the part of fuel cell that contributes current to the external circuit) versus the external load voltage (Fig. 9). For this specific SOFC unit, when the external load voltage is lower than 0.71 V, all segments of the fuel cell will be able to contribute current (and thus electrical energy) to the external circuit. As the external load voltage increases (over 0.71 V), the effective length of the fuel cell decreases with only a portion of the cell contributing current and useful energy. The effective length reaches zero when the external load voltage exceeds 1.1 V. Such property is very important in the optimization of a SOFC under specific loading conditions.

As shown in Eq. (5), the water vapor partial pressure plays an important role in the Nernst potential. In Fig. 10 we plot the relation between the external load voltage and the vapor partial pressure distribution along the longitudinal direction. Generally, the vapor partial pressure increases when the external load voltage decreases. Meanwhile, the vapor partial pressure increases along the flow direction. Indeed, lower external load voltage corresponds to higher current contribution (as

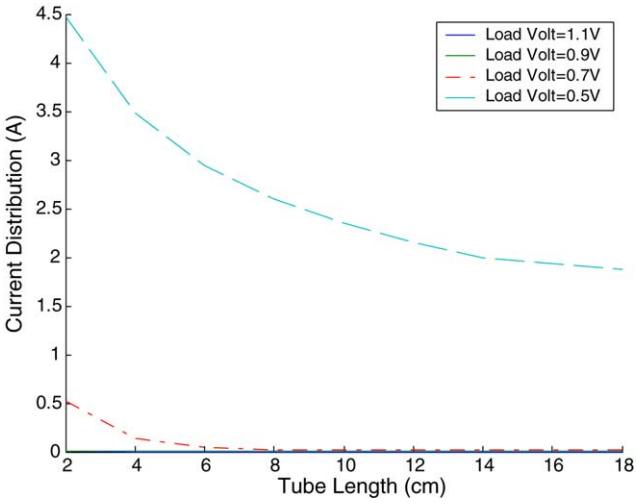

Fig. 8. Current contributions along the flow direction with different load voltage.

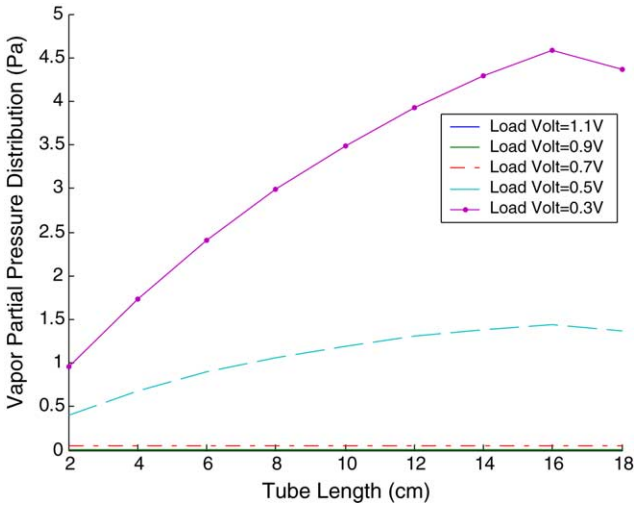

Fig. 10. Vapor partial pressure distribution along the flow direction.

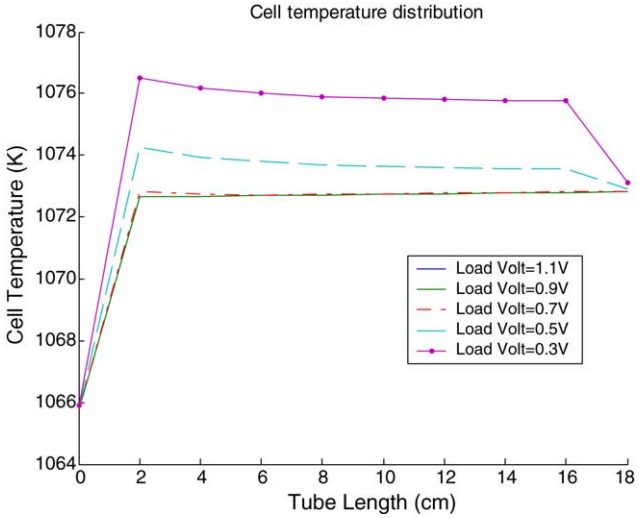

Fig. 11. Cell body temperature distribution along the longitudinal direction.

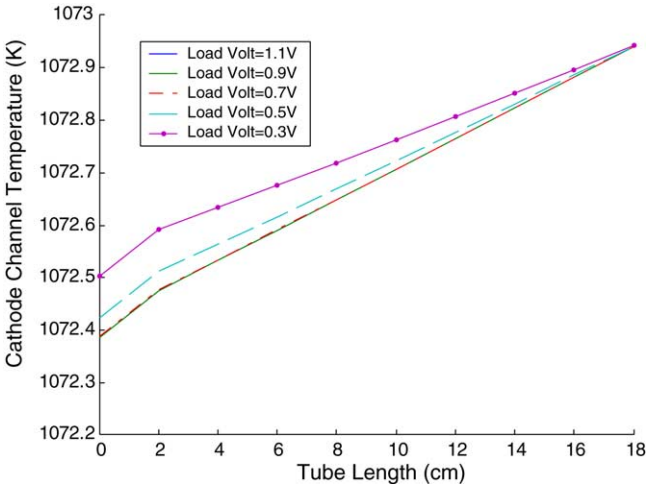

Fig. 13. Cathode channel temperature distribution along the flow direction.

illustrated in Fig. 8). As a result, the hydrogen/oxygen consumption increases and thus the vapor production increases, yielding higher vapor partial pressure. In the mean time, the heat produced by the electrochemical reaction and the three polarization resistances also increase, which lead to an increase in the fuel cell body temperature. Fig. 11 shows that the fuel cell temperature increases with a decrease of the load voltage. The increase of the cell body temperature, on the other hand, leads to the gas temperature increase along the flow direction for both anode and cathode channels, as shown in Figs. 12 and 13. It should be noted that the change in the temperature is generally insignificant. One interesting observation is that the change of gas temperature in the anode channel is more significant than that in the cathode channel. The reason is that while in the cathode channel both oxygen diffusion and heat convection occur, in the anode channel, besides the hydrogen diffusion and heat convection, the diffusion of the produced vapor also takes place. In the case that the PEN temperature is higher than that of the gases in the channels, the vapor diffusion will enforce the heat transfer between the PEN and the gases. Fig. 14 shows that the temperature distribution of the insulator is similar to those of the gases in the cathode channel. To illustrate the heat transfer effects to the PEN, the average heat flow rates towards the PEN for load cases 0.4 and 0.9 V are listed in Table 2. The

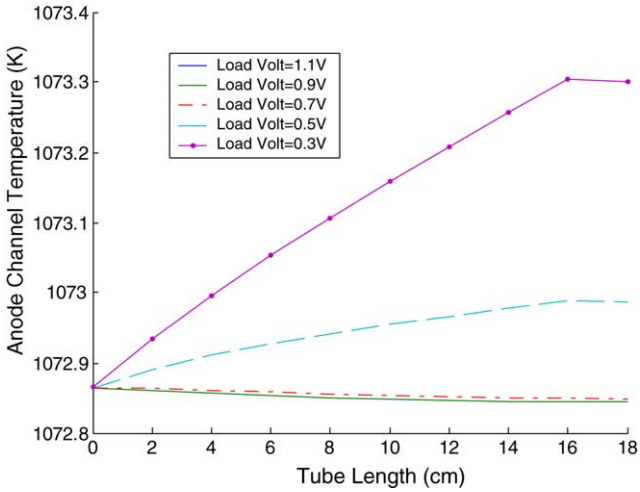

Fig. 12. Anode channel temperature distribution along the flow direction.

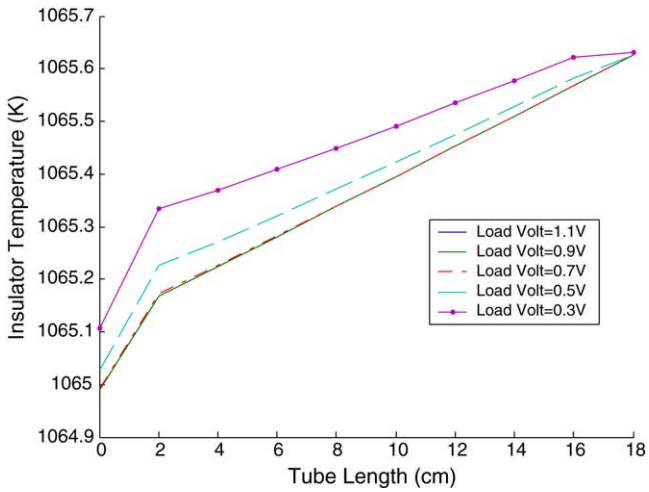

Fig. 14. Insulator temperature distribution along the flow direction.

Table 2
The average heat transfer to the PEN (W)

	Generation	Radiation	Anode/convection	Cathode/convection	Anode/diffusion	Cathode/diffusion
0.4 V	61.6625	−2.6101	−81.0218	−326.1931	−2.3537	3.8833
0.9 V	0.0134	−2.0952	94.3834	205.7795	−0.0006	0.0009

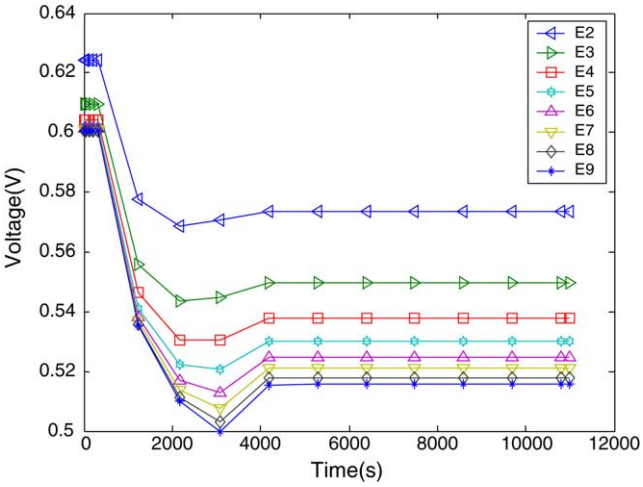

Fig. 15. Voltage contributions transient response.

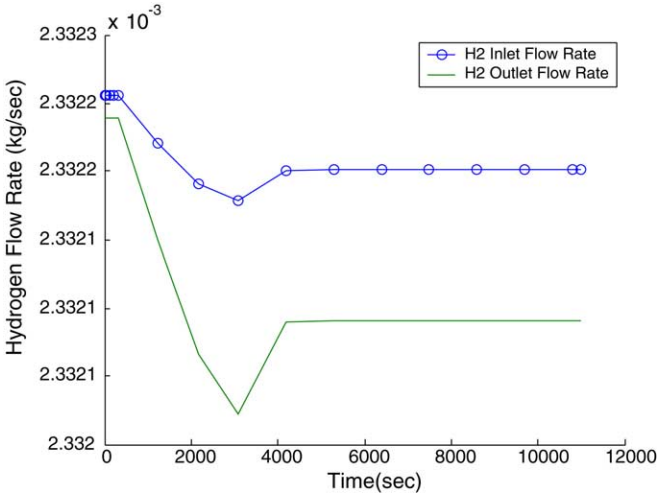

Fig. 17. Inlet/outlet hydrogen flow rate.

radiation and heat transfer due to mass diffusion are negligible as compared to the convective heat transfer. When the load voltage goes up from 0.4 to 0.9 V, the heat generation due to electrochemical reaction and the equivalent resistance decrease because the current contribution goes down, which decrease the PEN temperature and thus the heat transfer reverses the direction.

3.3. Transient behavior analysis

Finally an investigation of the system transient behavior is studied. Such transient behaviors are critical to SOFC control development. In general, the external load can be either load current or load voltage. In this study, we use external step voltage change (step load voltage experiencing sudden change from 0.6 to 0.5 V) and analyze the systems overall transient response. The inlet/outlet gas/fuel flow rates are controlled by using the traditional nozzle equation [16]. The flow rate coefficient of the nozzle usually depends on the temperature, pressure difference through the nozzle, flow rate itself, etc. To simplify the simulation, here we use constant flow rate coefficients (Table 1). The load goes down from 0.6 to 0.5 V after 500 s.

In Fig. 15, E2–E9 curves represent the time history of the Nernst potentials of the segmented sub-fuel cells. As the external load voltage goes down from 0.6 to 0.5 V, the Nernst potentials of all sub-fuel cells go down and show a slow transient part (about 1 h in the current simulation) with different magnitudes, and then go back to new steady-state values. The transient response in the Nernst potential is very complex, which is related to all parametric changes associated with the entire fuel cell activity. Since the Nernst potentials of all sub-cells are higher than the external load voltages, all sub-cells contribute current, as shown in Fig. 16. Generally, these results are in total agreement with the steady-state observations.

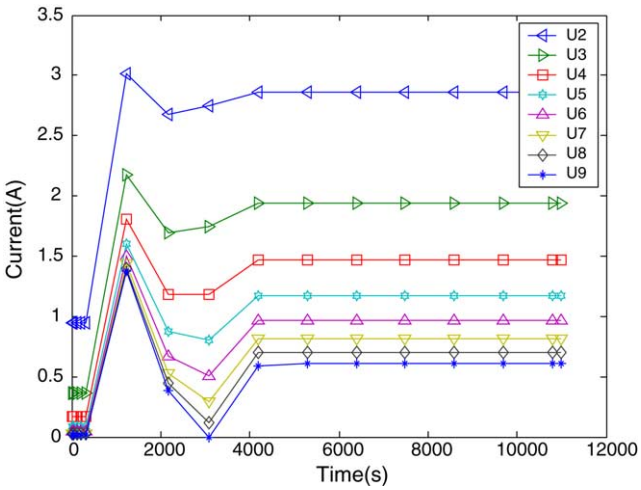

Fig. 16. Current contributions transient response.

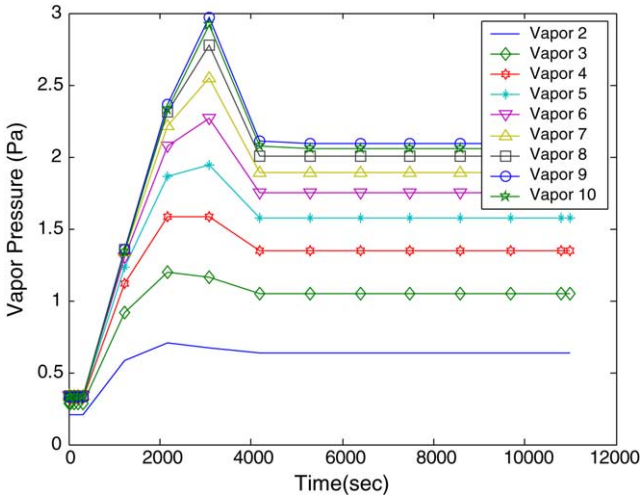

Fig. 18. Vapor partial pressure distribution transient response.

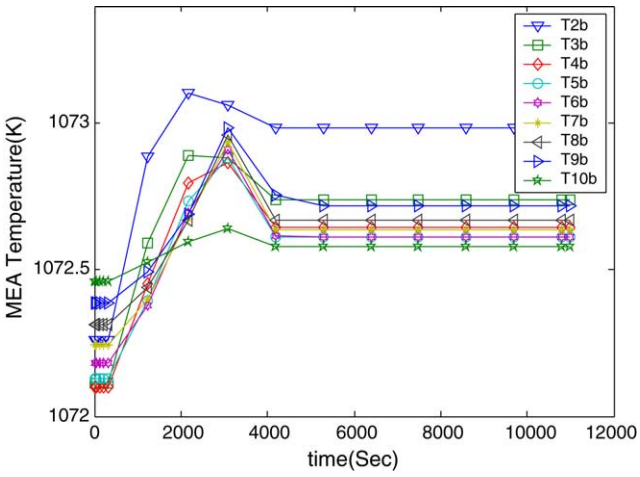

Fig. 19. Cell temperature distribution transient response.

After the load voltage experiences sudden change, there are overshoots in current contributions from sub-cells. Moreover, there are also (delayed) overshoots in both hydrogen consumption and vapor production, as shown in Figs. 17 and 18. The increase of vapor partial pressure reduces the inlet pressure difference, thus the inlet hydrogen flow rate goes down for a period of time. The decrease of inlet hydrogen flow rate and the increase of the hydrogen consumption will reduce the outlet hydrogen flow rate, as illustrated in Fig. 18. The peak (overshoot) of the current also increases the heat production and thus the PEN temperature increases (based on Eq. (4e)), as shown in Fig. 19. The increase of PEN temperature, on the other hand, increases the temperatures of the anode channel gas and the insulator, shown in Figs. 20 and 21. In Fig. 22 we plot the output power history of the fuel cell under step external load change.

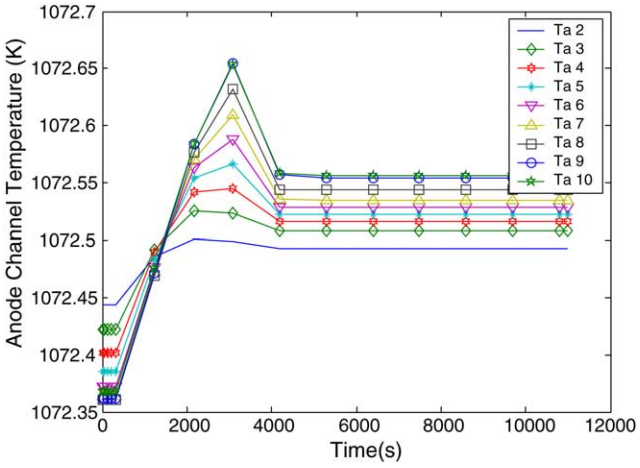

Fig. 20. Anode channel temperature distribution transient response.

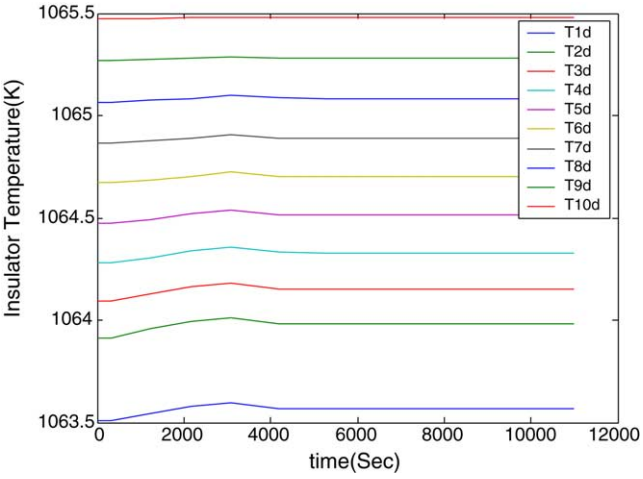

Fig. 21. Insulator temperature distribution transient response.

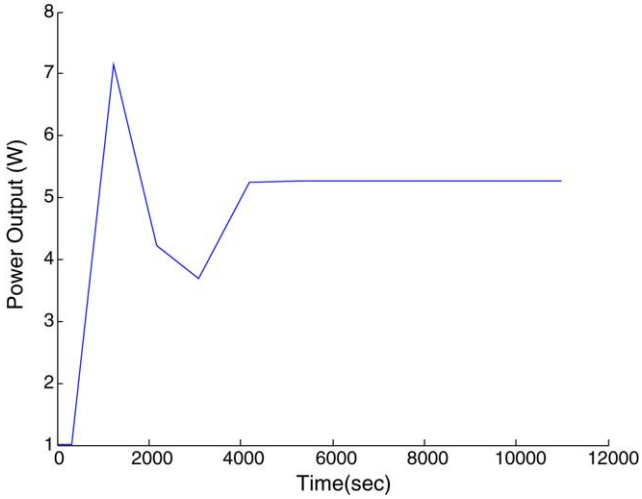

Fig. 22. Fuel cell output power.

4. Conclusions

In this paper, a dynamic model of a single tubular SOFC combining heat, species transportation and electrochemical reaction effects is developed to study its steady-state and transient behavior. The polarization performance and output power density are determined by a variety of interacting fuel cell state variables such as fuel/gas partial pressure distribution, heat transfer between cell body and gases. Due to the non-uniform distribution of the Nernst potential along the longitudinal direction, the external load voltage plays an important rule in the cell performance. When the Nernst potentials of some segments of the fuel cell are lower than the external load voltage, these segments will not be able to contribute current. A series of experimental and numerical studies are carried out to verify the model and explore the underlying dynamic behavior. This model can be readily used in system optimization and dynamic control.

Acknowledgements

This research is supported by US Army (Advanced Technology for Portable Miniature and Micro Fuel Cells, US

ARMY CECOM, Agreement No. DAAB07-03-3-K-415), the Connecticut Global Fuel Cell Center, and the University of Connecticut Research Foundation.

References

[1] Y. Du, N.M. Sammes, Fabrication and properties of anode-supported tubular solid oxide fuel cells, J. Power Sources 136 (2004) 66–71.
[2] J.W. Kim, A.V. Virkar, K. Fung, K. Mehta, S.C. Singhal, Polarization effects in intermediate temperature, anode-supported solid oxide fuel cell, J. Electrochem. Soc. 146 (1) (1999) 69–78.
[3] P. Li, M.K. Chyu, Simulation of the chemical/electrochemical reactions and heat/mass transfer for a tubular SOFC in a stack, J. Power Sources 124 (2003) 487–498.
[4] S. Nagata, A. Momma, T. Kato, Y. Kasuga, Numerical analysis of output characteristics of tubular SOFC with internal reformer, J. Power Sources 101 (2001) 60–71.
[5] C. Haynes, Simulating process settings for unslaved SOFC response to increases in load demand, J. Power Sources 109 (2002) 365–376.
[6] T. Ota, M. Koyama, C. Wen, K. Yamada, H. Takahashi, Object-based modeling of SOFC system: dynamic behavior of micro-tube SOFC, J. Power Sources 118 (2003) 430–439.
[7] R.J. Cooper, J. Billingham, A.C. King, Flow and reaction in solid oxide fuel cells, J. Fluid Mech. 411 (2000) 233–262.
[8] S. Krumdieck, S. Page, S. Round, Solid oxide fuel cell architecture and system design for secure power on an unstable grid, J. Power Source 125 (2004) 189–198.
[9] J. Yuan, M. Rokni, B. Sunden, Three-dimensional computational analysis of gas and heat transport phenomena in ducts relevant for anode-supported solid oxide fuel cells, Int. J. Heat Mass Transfer 46 (2003) 809–821.
[10] R.E. Sonntag, C. Borgnakke, G.J. Van Wylen, Fundamentals of Thermodynamics, 6th ed., Wiley, 2003.
[11] S.V. Patankar, Numerical Heat Transfer and Fluid Flow, Hemisphere, 1980.
[12] J.P. Holman, Heat Transfer, 8th ed., McGraw-Hill, 1997.
[13] E. Achenbach, Three-dimensional and time-dependent simulation of a planar solid oxide fuel cell stack, J. Power Sources 49 (1994) 333–348.
[14] L. Petruzzi, S. Cocchi, F. Fineschi, A global thermo-electrochemical model for SOFC systems design and engineering, J. Power Sources 118 (2003) 96–107.
[15] R.L. Boylestad, Electronic Devices and Circuit Theory, Prentice-Hall, 1987.
[16] J.T. Pukrushpan, H. Peng, A.G. Stefanopoulou, Control-oriented modeling and analysis for automotive fuel cell systems, ASME J. Dyn. Syst. Meas. Contr. 126 (2004) 14–24.